chemistry

MDPI

Article

Defects and Calcium Diffusion in Wollastonite

Sumudu Nimasha [1], Sashikesh Ganeshalingam [1], Navaratnarajah Kuganathan [2,3,*], Konstantinos Davazoglou [4] and Alexander Chroneos [2,3]

[1] Department of Chemistry, University of Jaffna, Sir. Pon Ramanathan Road, Thirunelvely, Jaffna 40000, Sri Lanka; nimashasumudu@gmail.com (S.N.); sashikesh@gmail.com (S.G.)
[2] Department of Materials, Imperial College London, London SW7 2AZ, UK; alexander.chroneos@imperial.ac.uk
[3] Faculty of Engineering, Environment and Computing, Coventry University, Priory Street, Coventry CV1 5FB, UK
[4] Department of Informatics and Telecommunications, National and Kapodistrian University of Athens, GR 15784 Athens, Greece; sdi1700026@di.uoa.gr
* Correspondence: n.kuganathan@imperial.ac.uk or ad0636@coventry.ac.uk

Received: 29 September 2020; Accepted: 28 October 2020; Published: 2 November 2020

Abstract: Wollastonite ($CaSiO_3$) is an important mineral that is widely used in ceramics and polymer industries. Defect energetics, diffusion of Ca ions and a solution of dopants are studied using atomistic-scale simulation based on the classical pair potentials. The energetically favourable defect process is calculated to be the Ca-Si anti-site defect cluster in which both Ca and Si swap their atomic positions simultaneously. It is calculated that the Ca ion migrates in the *ab* plane with an activation energy of 1.59 eV, inferring its slow diffusion. Favourable isovalent dopants on the Ca and Si sites are Sr^{2+} and Ge^{4+}, respectively. Subvalent doping by Al on the Si site is a favourable process to incorporate additional Ca in the form of interstitials in $CaSiO_3$. This engineering strategy would increase the capacity of this material.

Keywords: wollastonite; defects; diffusion; atomistic simulation; mineral

1. Introduction

Wollastonite is an important naturally occurring or synthetic mineral of great interest in the development of ceramics, plastics and paints [1–4]. This mineral is mainly found in the USA, India, Mexico, China, Turkey and Finland [5]. In general, a relatively small amount of impurities, such as Fe, Mg, Al and Sr, contaminate pure $CaSiO_3$ [6]. Owing to its remarkable physical, mechanical, electrical and thermal properties, this material has been used as a ceramic, an insulator, a filler and a polymer [2,7–12].

Though wollastonite is mined from ores for large-scale commercial applications, there are many experimental reports explaining the procedures of synthesising and characterising wollastonite in laboratories [1,5,10,13,14]. Abd Rashid et al. [1] used the solid-state reaction method at low temperature to produce wollastonite from limestone and silica sand and concluded that the resultant compound is expected to exhibit good physical properties due to the experimental density that is close to its theoretical value. The precipitation technique is the most common method that has been reported by several researchers to prepare wollastonite [15–18]. The sol–gel method is another technique that has been used to synthesise wollastonite by De La Casa-Lillo et al. [19], and the correlation between thermal treatment and bio activity has been discussed. In the literature, a few theoretical studies are available on wollastonite [20–23]. Edrees et al. [20] used density functional theory (DFT) simulations to analyse the structural, mechanical, optical and electronic properties of wollastonite. Atomistic simulations performed on the surface structures of wollastonite show that the stabilisation of the surface is due

to the adsorption of water in a dissociated form [21]. Longo et al. [22] used quantum mechanical simulations to show that the adsorption of CO_2 on the $CaSiO_3$ surface facilitates the formation of CO_3^{2-} ions due to the reaction between CO_2 and surface oxygen. DFT simulations performed by Profeta et al. [23] show that accurate ^{17}O NMR spectra should be calculated using hybrid functions. However, there are no experimental or theoretical studies on intrinsic defects, diffusion or dopants of wollastonite in the literature. The presence of defects in a material is important, as they influence its physical, mechanical and optical properties.

Atomistic simulation based on the pair-wise potentials is a powerful tool to examine the energetics of intrinsic defects, migration pathways and solutions of dopants in ionic materials. A wide range of oxide materials have been examined using this method to provide insight into defects, diffusion and dopants [24–28]. The present study systematically examined the intrinsic defect processes, Ca- ion diffusion and solution of divalent (Co, Mn, Ni, Mg, Zn, Sr and Ba), trivalent (Al, Ga In, Fe, Sc, Y, Gd and La) and tetravalent (Ga, Ti, Sn, Zr and Ce) dopants in $CaSiO_3$.

2. Computational Methods

A classical pair potential-based atomistic simulation, as implemented in the General Utility Lattice Program (GULP) code [29], was used to calculate defect, diffusion and dopant properties in $CaSiO_3$. Interactions between ions were modelled using long-range (Coulomb) and short-range (electron–electron repulsion and dispersive attraction) forces. Short-range forces were modelled using Buckingham potentials (refer to Table 1). Full geometry optimisation (cell parameters and ionic positions) was performed using the Broyden–Fletcher–Goldfarb–Shanno (BFGS) algorithm [30]. The Mott–Littleton approach was implemented to model the defects [31]. The diffusion of Ca ions was calculated considering two adjacent Ca vacancy sites as initial and final configurations. Seven atomic positions were selected between two adjacent Ca vacancy sites and they were allowed to relax. The activation energy is defined as the difference between the vacancy formation energy and the maximum energy along the diffusion path. In the current methodology, ions were fully charged and defect concentration was low. Nevertheless, relative energies and trends should be consistent [32].

Table 1. Buckingham potential parameters [33,34] used in the classical simulations of $CaSiO_3$. Two-body $[\Phi_{ij}(r_{ij}) = A_{ij} \exp(-r_{ij}/\rho_{ij}) - C_{ij}/r_{ij}^6]$, where A, ρ and C are parameters which were selected carefully to reproduce the experimental data. The values of Y and K represent the shell charges and spring constants. A very large spring constant means there is no shell charge and atom is treated as core.

Interaction	*A*/eV	*ρ*/Å	*C*/eV·Å^6	Y/e	K/eV·Å^{-2}
Ca^{2+}–O^{2-}	1090.40	0.3372	0.00	1.260	34.0
Si^{4+}–O^{2-}	1283.91	0.32052	10.66	4.000	99999.0
O^{2-}–O^{2-}	22764.30	0.1490	27.89	−2.86	74.92

3. Results

3.1. Crystal Structure of $CaSiO_3$ and Validation of Potentials

The crystal structure of $CaSiO_3$ is monoclinic [space group $P2_1/a$ (no: 14)] with the experimental lattice parameters a = 15.41 Å, b = 7.32 Å, c = 7.06 Å, $\alpha = \gamma = 90°$ and $\beta = 95.3°$ [35]. Ca ions form a distorted octahedral structure and Si atoms form tetrahedral units. SiO_4 tetrahedral units are inter-connected by corner sharing (refer to Figure 1). Geometry optimisation was performed under constant pressure to get equilibrium lattice constants and compare them with experimental values to validate the potentials used in this study. Calculated lattice parameters are reported in Table 2. There was a good agreement between calculated and experimental values.

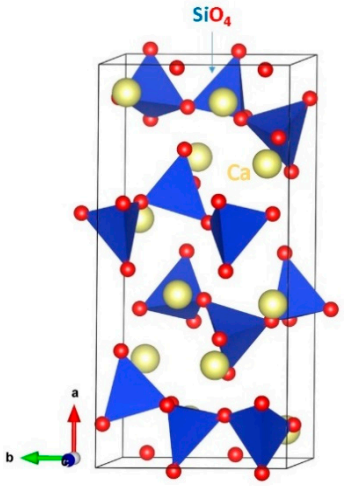

Figure 1. Crystal structure of $CaSiO_3$.

Table 2. Calculated and experimental structural parameters of $CaSiO_3$. Percentage difference between the calculated and the experimental value (**Δ**) is also provided.

Parameter	Calculated	Experiment [35]	|Δ|(%)
a (Å)	15.23	15.41	1.17
b (Å)	7.30	7.32	0.24
c (Å)	7.01	7.06	0.76
α (°)	90.0	90.0	0.00
β (°)	91.5	95.3	3.96
γ (°)	90.0	90.0	0.00
V ($Å^3$)	779.39	793.47	1.77

3.2. Defect Energetics

In this section, we discuss the energetics of key defect processes in $CaSiO_3$. Point defect (vacancies and interstitials) energies were first calculated and then they were combined to calculate Schottky and Frenkel energies. Anti-site defects in which Ca and Si swap their atomic positions were also calculated in the form of isolated and cluster. The following equations in Kröger–Vink notation [36] describe the Schottky, Frenkel and anti-site defect process.

$$\text{Ca Frenkel}: \ \mathrm{Ca}_{\mathrm{Ca}}^{\mathrm{X}} \rightarrow V_{\mathrm{Ca}}^{''} + \mathrm{Ca}_{\mathrm{i}}^{\bullet\bullet} \tag{1}$$

$$\text{Si Frenkel}: \ V_{\mathrm{Si}}^{\mathrm{X}} \rightarrow V_{\mathrm{Si}}^{''''} + \mathrm{Si}_{\mathrm{i}}^{\bullet\bullet\bullet\bullet} \tag{2}$$

$$\text{O Frenkel}: \ \mathrm{O}_{\mathrm{O}}^{\mathrm{X}} \rightarrow V_{\mathrm{O}}^{\bullet\bullet} + \mathrm{O}_{\mathrm{i}}^{''} \tag{3}$$

$$\text{Schottky}: \ \mathrm{Ca}_{\mathrm{Ca}}^{\mathrm{X}} + \mathrm{Si}_{\mathrm{Si}}^{\mathrm{X}} + 3\,\mathrm{O}_{\mathrm{O}}^{\mathrm{X}} \rightarrow V_{\mathrm{Ca}}^{''} + V_{\mathrm{Si}}^{''''} + 3\,V_{\mathrm{O}}^{\bullet\bullet} + \mathrm{CaSiO_3} \tag{4}$$

$$\text{CaO Schottky}: \ \mathrm{Ca}_{\mathrm{Ca}}^{\mathrm{X}} + \mathrm{O}_{\mathrm{O}}^{\mathrm{X}} \rightarrow V_{\mathrm{Ca}}^{''} + V_{\mathrm{O}}^{\bullet\bullet} + \mathrm{CaO} \tag{5}$$

$$\mathrm{SiO_2}\ \text{Schottky}: \ \mathrm{Si}_{\mathrm{Si}}^{\mathrm{X}} + 2\,\mathrm{O}_{\mathrm{O}}^{\mathrm{X}} \rightarrow V_{\mathrm{Si}}^{''''} + 2\,V_{\mathrm{O}}^{\bullet\bullet} + \mathrm{SiO_2} \tag{6}$$

$$\text{Ca/Si antisite (isolated)}: \ \mathrm{Ca}_{\mathrm{Ca}}^{\mathrm{X}} + \mathrm{Si}_{\mathrm{Si}}^{\mathrm{X}} \rightarrow \mathrm{Ca}_{\mathrm{Si}}^{''} + \mathrm{Si}_{\mathrm{Ca}}^{\bullet\bullet} \tag{7}$$

$$\text{Ca/Si antisite (cluster)}: \ \mathrm{Ca}_{\mathrm{Ca}}^{\mathrm{X}} + \mathrm{Si}_{\mathrm{Si}}^{\mathrm{X}} \rightarrow \left\{\mathrm{Ca}_{\mathrm{Si}}^{''} : \mathrm{Si}_{\mathrm{Ca}}^{\bullet\bullet}\right\}^{\mathrm{X}} \tag{8}$$

Figure 2 reports the defect reaction energies. The Frenkel energies are important, as they influence the diffusion properties of the material. Furthermore, a low Frenkel energy is associated with the high concentration of point defects, leading to the loss of the crystal structure. The oxygen Frenkel energy is the lowest energy (2.33 eV) process among the other Frenkel energies. The Si Frenkel energy (8.95 eV) is significantly higher than the Ca Frenkel energy (3.46 eV). This is due to the introduction of highly charged defects (V''''_{Si} and $Si_i^{\bullet\bullet\bullet\bullet}$) in the lattice. The formation of Schottky defects is endoergic by 3.58 eV, meaning that this defect is unfavourable. The formation of CaO and SiO_2 via CaO Schottky and SiO_2 Schottky processes, respectively, was also considered. Their defect energies are also highly endothermic. Finally, the Ca/Si anti-site defect was considered. The cluster form of this defect exhibits lower energy than its isolated form. This is because of the unstable nature of isolated defects (Ca''_{Si} and $Si^{\bullet\bullet}_{Ca}$) aggregating to form clusters with a binding energy of −2.53 eV. The anti-site defect has been observed in many oxide materials during the cycling of as-prepared materials and synthesis at high temperatures and pressures [37–39]. This defect has also been observed in previous theoretical studies [40–43].

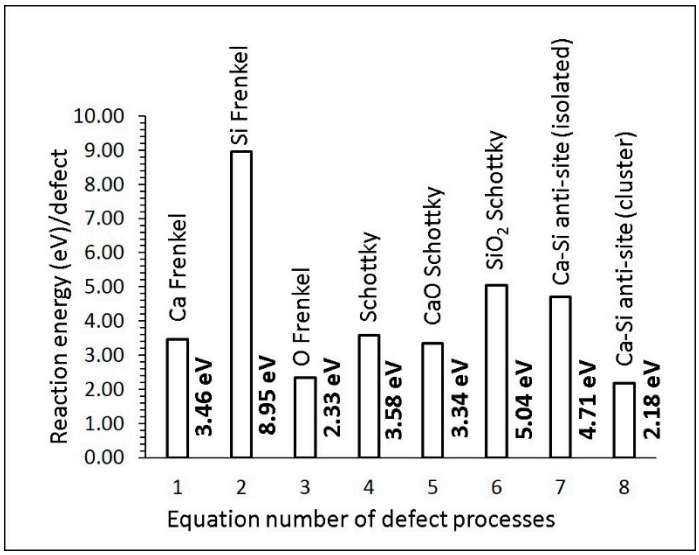

Figure 2. Defect energies for different defect processes, as shown in the above equations.

3.3. Calcium Ion Diffusion

The performance of a material can be influenced by its diffusion properties, which are associated with the activation energy and pre-exponential factor of the Arrhenius equation and energetics of point defects. The present methodology is an appropriate tool to calculate the activation energies of long-range diffusion pathways of Ca ions. The results presented here would be beneficial to the experimentalist as the determination of ion pathways and activation energies can be challenging experimentally. In previous modelling studies with this classical approach, many oxides have been examined and diffusion properties reported [27,44–46]. For example, the diffusion pathway calculated in $LiFePO_4$ by Fisher et al. [47] is in excellent agreement with the neutron diffraction study reported by Nishimura et al. [48].

In general, Ca ion diffusion in Ca-bearing oxide materials is expected to be sluggish due to its ions with double positive charge. In previous theoretical simulations based on the DFT and classical pair potentials, it was shown that activation energies of Ca ion diffusion in Ca-based minerals are high, confirming the slow diffusion [49–52].

We identified four different local Ca hops (A, B, C and D) and their vacancy-assisted migration pathways were calculated (refer to Figure 3). Table 3 reports the local Ca hops with their distances and corresponding activation energies.

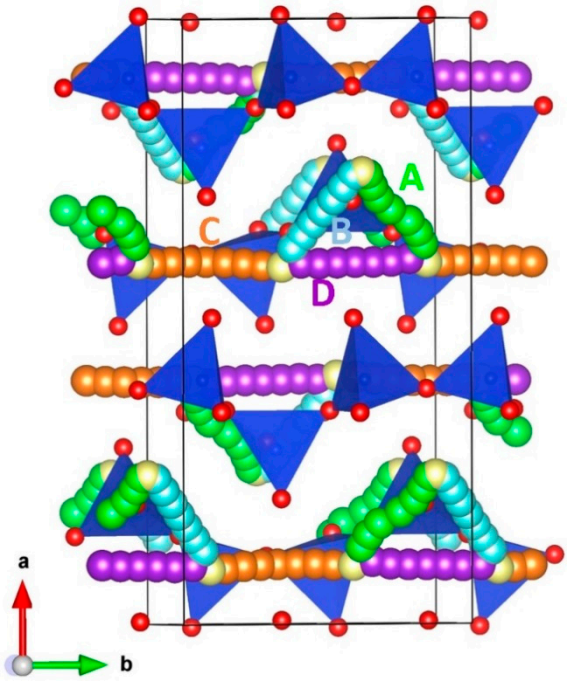

Figure 3. Long-range Ca vacancy migration paths considered. Green, light blue, orange and purple atoms show the Ca ion movement in different local Ca hops.

Table 3. Activation energies calculated for local Ca hops.

Hop	Ca–Ca Distance (Å)	Activation Energy (eV)
A	3.46	1.37
B	3.49	1.59
C	3.63	1.34
D	3.67	2.02

The local hop A exhibits the lowest activation energy. The activation energy calculated for the local hop B is slightly higher by 0.03 eV than that calculated for the local hop A. The highest activation energy is noted for the local hop D. In order to find the long-range diffusion pathways, local hops were connected. Three possible long-range diffusion pathways were identified (refer to Table 4). The lowest energy long-range diffusion pathway is A↔B↔C↔A↔B with an activation energy of 1.59 eV, inferring the slow diffusion. The movement of Ca ions is observed in the *ab* plane. Figure 4 shows the energy profile diagrams for local hops.

Table 4. Long-range Ca ion diffusion paths and their activation energies.

Long-Range Path	Activation Energy (eV)
C↔D↔C↔D↔C	2.02
A↔B↔C↔A↔B	1.59
A↔B↔C↔D↔C	2.02

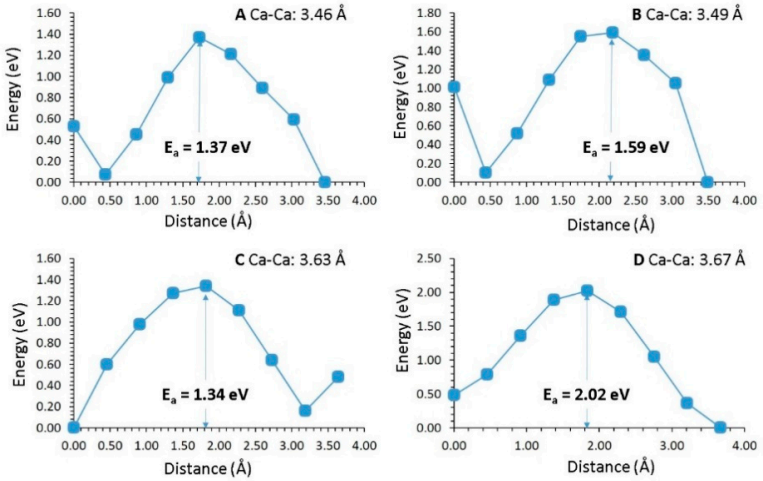

Figure 4. Energy profile diagrams calculated for four different local Ca hops, as shown in Figure 3.

3.4. Solution of Dopants

Dopants play a significant role in tailoring the properties of a material. In particular, dopants with different sizes or charges compared to the host atoms will affect the properties of the host compound. Here, we considered a variety of isovalent and aliovalent dopants for screening and predicting promising dopants that can be verified and further explored experimentally. Solution energies were calculated using appropriate charge compensation defects and lattice energies. The Supplementary Materials provide the Buckingham potentials used for dopants (refer to Table S1).

3.4.1. Divalent Dopants

First, the Ca site was considered to dope divalent dopants (M = Co, Mn, Ni, Mg, Zn, Sr and Ba). The solution energy was calculated using the following equation.

$$MO + Ca_{Ca}^{X} \rightarrow M_{Ca}^{X} + CaO \quad (9)$$

Exothermic solution energy (−0.03 eV) was calculated for Sr^{2+}, suggesting that it is the most favourable dopant on the Ca site (refer to Figure 5). A possible composition that can be prepared by experiment is $Ca_{1-x}Sr_xSiO_3$ ($0.0 < x < 1.0$). The second most stable dopant is Ba^{2+}, with a solution energy of 0.16 eV. Other dopants exhibit high endoergic solution energies, meaning that they are unlikely to be doped at room temperature. The high preference of Sr^{2+} could be due to its ionic radius (1.18 Å), which is close to the ionic radius of Ca^{2+} (1.00 Å).

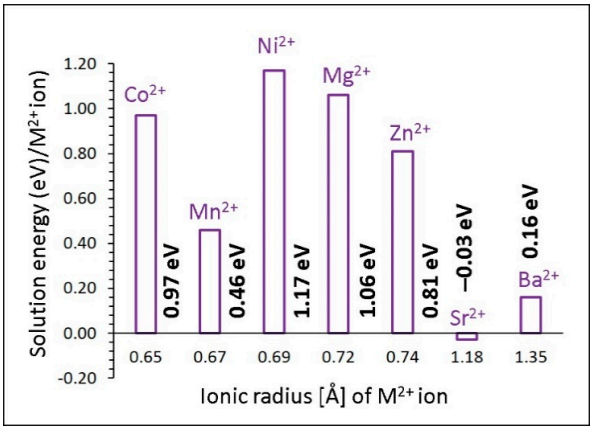

Figure 5. Solution energy of MO (R = Co, Mn, Ni, Mg, Zn, Sr and Ba) with respect to the M^{2+} ionic radius.

3.4.2. Trivalent Dopants

The doping of trivalent cations (Al^{3+}, Ga^{3+}, In^{3+}, Fe^{3+}, Sc^{3+}, Y^{3+}, Gd^{3+} and La^{3+}) was considered on the Si site. In this doping process, Ca interstitials were introduced to compensate the negatively charged lattice. This process can increase the capacity of $CaSiO_3$ and enhance the diffusion of Ca ions. The following equation was used to calculate the solution energy for this process.

$$M_2O_3 + 2Si_{Si}^{X} + CaO \rightarrow 2\,M'_{Si} + Ca_i^{\bullet\bullet} + 2\,SiO_2 \quad (10)$$

Calculated solution enthalpies are reported in Figure 6. The most favourable dopant for this process is Al^{3+}, with a solution energy of 3.47 eV, though the solution is endoergic. The possible composition that can be prepared by experiment would be $Ca_{1+x}Al_xSi_{1-x}O_8$ ($0.0 < x < 1.0$). The second most favourable dopant is Fe^{3+}. High solution energies (>4 eV) are calculated for the other dopants, meaning they are unlikely to take place at room temperature.

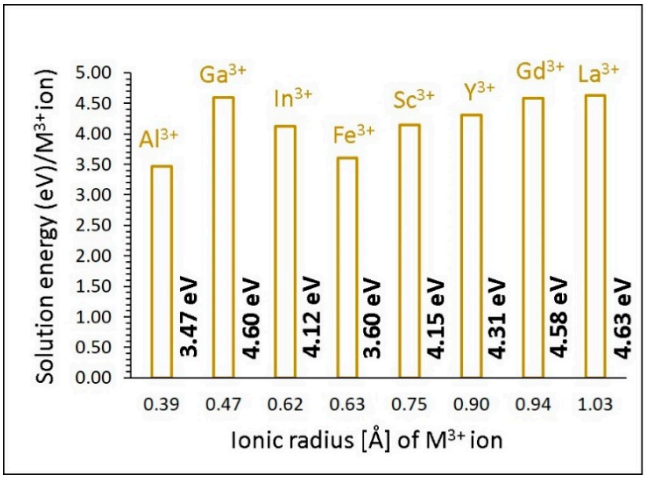

Figure 6. Solution energy of M_2O_3 (M = Co, Mn, Ni, Mg, Zn, Sr and Ba) with respect to the M^{3+} ionic radius.

3.4.3. Tetravalent Dopants

Finally, tetravalent cations (Ge^{4+}, Ti^{4+}, Sn^{4+}, Zr^{4+} and Ce^{4+}) were considered on the Si site. Solution energy was calculated using the following reaction equation.

$$MO_2 + Si_{Si}^{X} \rightarrow M_{Si}^{X} + SiO_2 \quad (11)$$

Solution energies are reported in Figure 7. The promising dopant for this process is Ge^{4+}. The preference of Ge^{4+} is due to the ionic radius of Si^{4+} (0.26 Å), which is close to the ionic radius of Ge^{4+} (0.39 Å). Endothermic solution energy shows that this process requires energy in the form of heat. This is due to the stronger Si-O bonds as compared to the Ge-O bonds. The second most favourable dopant is Ti^{4+}. Its solution energy is higher only by 0.07 eV than that calculated for Ge^{4+}. High solution energies are calculated for the other dopants. In particular, solution energies for ZrO_2 and CeO_2 are 2.37 eV and 3.30 eV, respectively, suggesting that they are unlikely to occur at room temperature.

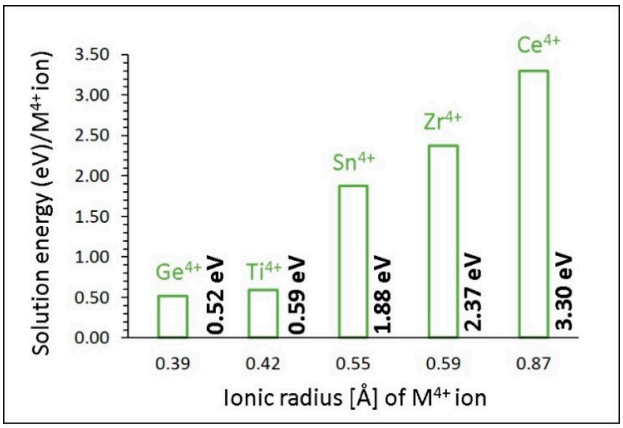

Figure 7. Solution energy of MO_2 (M = Ge, Ti, Sn, Zr and Ce) with respect to the M^{4+} ionic radius.

4. Conclusions

In this study, an atomistic simulation based on the classical potentials was applied to examine the intrinsic defect processes, vacancy-assisted Ca ion diffusion and solution of dopants in $CaSiO_3$. The Ca-Si anti-site defect cluster was calculated to be the lowest energy process, meaning that a small amount of Ca on the Si site and Si on the Ca site will be present, particularly at higher temperatures. The long-range vacancy-assisted Ca ion migration pathway is in the *ab* plane with an activation energy of 1.59 eV, inferring slow diffusion. The promising dopant on the Si site to increase the Ca content in $CaSiO_3$ is Al^{3+}. Promising isovalent dopants on the Ca and Si sites are Sr^{2+} and Ge^{4+}, respectively, and these dopants can prevent phase transformation.

Supplementary Materials: The following are available online at http://www.mdpi.com/2624-8549/2/4/59/s1, Table S1: Interatomic potential parameters used in the atomistic simulations of $CaSiO_3$.

Author Contributions: Computation, S.N. and N.K.; writing, N.K. and S.N.; analysis and editing, N.K., S.G., K.D. and A.C. All authors have read and agreed to the published version of the manuscript.

Funding: This research received no external funding.

Acknowledgments: High-performance facilities were provided by Imperial College London, Coventry University and the University of Jaffna.

Conflicts of Interest: The authors declare no conflict of interest.

References

1. Abd Rashid, R.; Shamsudin, R.; Abdul Hamid, M.A.; Jalar, A. Low temperature production of wollastonite from limestone and silica sand through solid-state reaction. *J. Asian Ceram. Soc.* **2014**, *2*, 77–81. [CrossRef]
2. Demidenko, N.I.; Podzorova, L.I.; Rozanova, V.S.; Skorokhodov, V.A.; Shevchenko, V.Y. Wollastonite as a New Kind of Natural Material (A Review). *Glass Ceram.* **2001**, *58*, 308–311. [CrossRef]
3. Kangal, M.O.; Bulut, G.; Guven, O. Physicochemical Characterization of Natural Wollastonite and Calcite. *Minerals* **2020**, *10*, 228. [CrossRef]
4. Serghiou, G.C.; Hammack, W.S. Pressure-induced amorphization of wollastonite ($CaSiO_3$) at room temperature. *J. Chem. Phys.* **1993**, *98*, 9830–9834. [CrossRef]
5. Kotsis, I.; Balogh, A. Synthesis of wollastonite. *Ceram. Int.* **1989**, *15*, 79–85. [CrossRef]
6. Svensson, K.; Neumann, A.; Menezes, F.F.; Lempp, C.; Pöllmann, H. The Conversion of Wollastonite to $CaCO_3$ Considering Its Use for CCS Application as Cementitious Material. *Appl. Sci.* **2018**, *8*, 304. [CrossRef]
7. Harabi, A.; Chehlatt, S. Preparation process of a highly resistant wollastonite bioCeramics using local raw materials: Effect of B_2O_3 additions on sintering and mechanical properties. *J. Therm. Anal. Calorim.* **2013**, *111*, 203–211. [CrossRef]
8. Ismail, H.; Shamsudin, R.; Abdul Hamid, M.A.; Jalar, A. Synthesis and characterization of nano-wollastonite from rice husk ash and limestone. *Mater. Sci. Forum* **2013**, *756*, 43–47. [CrossRef]

9. Lin, K.; Chang, J.; Lu, J. Synthesis of wollastonite nanowires via hydrothermal microemulsion methods. *Mater. Lett.* **2006**, *60*, 3007–3010. [CrossRef]
10. Yun, Y.H.; Yun, S.D.; Park, H.R.; Lee, Y.K.; Youn, Y.N. Preparation of β-wollastonite glass-Ceramics. *J. Mater. Synth. Process.* **2002**, *10*, 205–209. [CrossRef]
11. Ming, H.; Ren, Z.S.; Hua, Z.X. Characterization and analysis of CaO-SiO_2-B_2O_3 ternary system Ceramics. *J. Mater. Sci. Mater. Electron.* **2011**, *22*, 389–393. [CrossRef]
12. Zilles, J.U. Wollastonites. In *Encyclopedia of Polymers and Composites*; Palsule, S., Ed.; Springer: Berlin/Heidelberg, Germany, 2013; pp. 1–21.
13. Gineika, A.; Siauciunas, R.; Baltakys, K. Synthesis of wollastonite from AlF_3-rich silica gel and its hardening in the CO_2 atmosphere. *Sci. Rep.* **2019**, *9*, 18063. [CrossRef] [PubMed]
14. Zulumyan, N.; Mirgorodski, A.; Isahakyan, A.; Beglaryan, H.; Gabrielyan, A.; Terzyan, A. A low-temperature method of the β-wollastonite synthesis. *J. Therm. Anal. Calorim.* **2015**, *122*, 97–104. [CrossRef]
15. Wan, X.; Chang, C.; Mao, D.; Jiang, L.; Li, M. Preparation and in vitro bioactivities of calcium silicate nanophase materials. *Mater. Sci. Eng. C* **2005**, *25*, 455–461. [CrossRef]
16. Long, L.H.; Chen, L.D.; Bai, S.Q.; Chang, J.; Lin, K.L. Preparation of dense β-CaSiO3 Ceramics with high mechanical strength and HAp formation ability in simulated body fluid. *J. Eur. Ceram. Soc.* **2006**, *26*, 1701–1706. [CrossRef]
17. Hazar, A.B.Y. Preparation and in vitro bioactivity of $CaSiO_3$ powders. *Ceram. Int.* **2007**, *33*, 687–692. [CrossRef]
18. Zhao, S.; Zhou, Z.; Wu, J.; Wang, S.; Guo, X.; Zhang, Q. Preparation and characterization of a novel hydroxyapatite-wollastonite/silk fibroin composite. *J. Compos. Mater.* **2011**, *46*, 1571–1581. [CrossRef]
19. De La Casa-Lillo, M.A.; Velásquez, P.; De Aza, P.N. Influence of thermal treatment on the "in vitro" bioactivity of wollastonite materials. *J. Mater. Sci. Mater. Med.* **2011**, *22*, 907–915. [CrossRef]
20. Edrees, S.J.; Shukur, M.M.; Obeid, M.M. First-principle analysis of the structural, mechanical, optical and electronic properties of wollastonite monoclinic polymorph. *Comput. Condens. Matter.* **2018**, *14*, 20–26. [CrossRef]
21. Kundu, T.K.; Hanumantha Rao, K.; Parker, S.C. Atomistic simulation of the surface structure of wollastonite. *Chem. Phys. Lett.* **2003**, *377*, 81–92. [CrossRef]
22. Longo, R.C.; Cho, K.; Brüner, P.; Welle, A.; Gerdes, A.; Thissen, P. Carbonation of Wollastonite (001) Competing Hydration: Microscopic Insights from Ion Spectroscopy and Density Functional Theory. *ACS Appl. Mater. Interfaces* **2015**, *7*, 4706–4712. [CrossRef] [PubMed]
23. Profeta, M.; Benoit, M.; Mauri, F.; Pickard, C.-J. First-Principles Calculation of the 17O NMR Parameters in Ca Oxide and Ca Aluminosilicates: The Partially Covalent Nature of the Ca-O Bond, a Challenge for Density Functional Theory. *J. Am. Chem. Soc.* **2004**, *126*, 12628–12635. [CrossRef] [PubMed]
24. Kuganathan, N.; Iyngaran, P.; Vovk, R.; Chroneos, A. Defects, dopants and Mg diffusion in $MgTiO_3$. *Sci. Rep.* **2019**, *9*, 4394. [CrossRef]
25. Kuganathan, N.; Kordatos, A.; Chroneos, A. Defect Chemistry and Li-ion Diffusion in Li_2RuO_3. *Sci. Rep.* **2019**, *9*, 550. [CrossRef] [PubMed]
26. Jay, E.E.; Rushton, M.J.D.; Chroneos, A.; Grimes, R.W.; Kilner, J.A. Genetics of superionic conductivity in lithium lanthanum titanates. *Phys. Chem. Chem. Phys.* **2015**, *17*, 178–183. [CrossRef]
27. Islam, M.S.; Fisher, C.A.J. Lithium and sodium battery cathode materials: Computational insights into voltage, diffusion and nanostructural properties. *Chem. Soc. Rev.* **2014**, *43*, 185–204. [CrossRef]
28. Kendrick, E.; Islam, M.S.; Slater, P.R. Atomic-scale mechanistic features of oxide ion conduction in apatite-type germanates. *Chem. Commun.* **2008**, 715–717. [CrossRef] [PubMed]
29. Gale, J.D. GULP: A computer program for the symmetry-adapted simulation of solids. *J. Chem. Soc. Faraday Trans.* **1997**, *93*, 629–637. [CrossRef]
30. Gale, J.D.; Rohl, A.L. The General Utility Lattice Program (GULP). *Mol. Simul.* **2003**, *29*, 291–341. [CrossRef]
31. Mott, N.F.; Littleton, M.J. Conduction in polar crystals. I. Electrolytic conduction in solid salts. *Trans. Faraday Soc.* **1938**, *34*, 485–499. [CrossRef]
32. Grimes, R.W.; Busker, G.; McCoy, M.A.; Chroneos, A.; Kilner, J.A.; Chen, S.-P. The Effect of Ion Size on Solution Mechanism and Defect Cluster Geometry. *Ber. Bunsenges. Phys. Chem.* **1997**, *101*, 1204–1210. [CrossRef]
33. Lewis, G.V.; Catlow, C.R.A. Potential models for ionic oxides. *J. Phys. C Solid State Phys.* **1985**, *18*, 1149–1161. [CrossRef]

34. Kuganathan, N.; Islam, M.S. Li_2MnSiO_4 Lithium Battery Material: Atomic-Scale Study of Defects, Lithium Mobility, and Trivalent Dopants. *Chem. Mater.* **2009**, *21*, 5196–5202. [CrossRef]
35. Hesse, K.F. Refinement of the crystal structure of wollastonite-2M (parawollastonite). *Z. Krist. Cryst. Mater.* **1984**, *168*, 93–98. [CrossRef]
36. Kröger, F.A.; Vink, H.J. Relations between the Concentrations of Imperfections in Crystalline Solids. In *Solid State Physics*; Seitz, F., Turnbull, D., Eds.; Academic Press: Cambridge, MA, USA, 1956; Volume 3, pp. 307–435.
37. Armstrong, A.R.; Kuganathan, N.; Islam, M.S.; Bruce, P.G. Structure and Lithium Transport Pathways in Li_2FeSiO_4 Cathodes for Lithium Batteries. *J. Am. Chem. Soc.* **2011**, *133*, 13031–13035. [CrossRef]
38. Kempaiah Devaraju, M.; Duc Truong, Q.; Hyodo, H.; Sasaki, Y.; Honma, I. Synthesis, characterization and observation of antisite defects in $LiNiPO_4$ nanomaterials. *Sci. Rep.* **2015**, *5*, 11041. [CrossRef]
39. Politaev, V.V.; Petrenko, A.A.; Nalbandyan, V.B.; Medvedev, B.S.; Shvetsova, E.S. Crystal structure, phase relations and electrochemical properties of monoclinic Li_2MnSiO_4. *J. Solid State Chem.* **2007**, *180*, 1045–1050. [CrossRef]
40. Kuganathan, N.; Kordatos, A.; Kelaidis, N.; Chroneos, A. Defects, Lithium Mobility and Tetravalent Dopants in the Li_3NbO_4 Cathode Material. *Sci. Rep.* **2019**, *9*, 2192. [CrossRef]
41. Kuganathan, N.; Kordatos, A.; Anurakavan, S.; Iyngaran, P.; Chroneos, A. Li_3SbO_4 lithium-ion battery material: Defects, lithium ion diffusion and tetravalent dopants. *Mater. Chem. Phys.* **2019**, *225*, 34–41. [CrossRef]
42. Gardiner, G.R.; Islam, M.S. Anti-Site Defects and Ion Migration in the $LiFe_{0.5}Mn_{0.5}PO_4$ Mixed-Metal Cathode Material. *Chem. Mater.* **2010**, *22*, 1242–1248. [CrossRef]
43. Islam, M.S.; Driscoll, D.J.; Fisher, C.A.J.; Slater, P.R. Atomic-Scale Investigation of Defects, Dopants, and Lithium Transport in the $LiFePO_4$ Olivine-Type Battery Material. *Chem. Mater.* **2005**, *17*, 5085–5092. [CrossRef]
44. Zhang, X.; Rui, X.; Chen, D.; Tan, H.; Yang, D.; Huang, S.; Yu, Y. $Na_3V_2(PO_4)_3$: An advanced cathode for sodium-ion batteries. *Nanoscale* **2019**, *11*, 2556–2576. [CrossRef] [PubMed]
45. Eames, C.; Frost, J.M.; Barnes, P.R.F.; O'Regan, B.C.; Walsh, A.; Islam, M.S. Ionic transport in hybrid lead iodide perovskite solar cells. *Nat. Commun.* **2015**, *6*, 7497. [CrossRef] [PubMed]
46. Malavasi, L.; Fisher, C.A.J.; Islam, M.S. Oxide-ion and proton conducting electrolyte materials for clean energy applications: Structural and mechanistic features. *Chem. Soc. Rev.* **2010**, *39*, 4370–4387. [CrossRef] [PubMed]
47. Fisher, C.A.J.; Hart Prieto, V.M.; Islam, M.S. Lithium Battery Materials $LiMPO_4$ (M = Mn, Fe, Co, and Ni): Insights into Defect Association, Transport Mechanisms, and Doping Behavior. *Chem. Mater.* **2008**, *20*, 5907–5915. [CrossRef]
48. Nishimura, S.-I.; Kobayashi, G.; Ohoyama, K.; Kanno, R.; Yashima, M.; Yamada, A. Experimental visualization of lithium diffusion in $LixFePO_4$. *Nat. Mater.* **2008**, *7*, 707. [CrossRef] [PubMed]
49. Torres, A.; Luque, F.J.; Tortajada, J.; Arroyo-de Dompablo, M.E. Analysis of Minerals as Electrode Materials for Ca-based Rechargeable Batteries. *Sci. Rep.* **2019**, *9*, 9644. [CrossRef]
50. Kuganathan, N.; Ganeshalingam, S.; Chroneos, A. Defect, transport, and dopant properties of andradite garnet $Ca_3Fe_2Si_3O_{12}$. *AIP Adv.* **2020**, *10*, 075004. [CrossRef]
51. Kuganathan, N.; Chroneos, A. Defects and Dopants in $CaFeSi_2O_6$: Classical and DFT Simulations. *Energies* **2020**, *13*, 1285. [CrossRef]
52. Dompablo, M.E.A.-D.; Krich, C.; Nava-Avendaño, J.; Biškup, N.; Palacín, M.R.; Bardé, F. A Joint Computational and Experimental Evaluation of $CaMn_2O_4$ Polymorphs as Cathode Materials for Ca Ion Batteries. *Chem. Mater.* **2016**, *28*, 6886–6893. [CrossRef]